J Mater Sci: Mater Electron (2023) 34:1605

Design and synthesis of 4,5-diazafluorene ligands and their ruthenium (II) complexes for photoresponse performance on organic photodiodes

Esma Yenel[1], Murat Yildirim[2,*], Caner Cebeci[3], Ibrahim Erden[3,*], Adem Kocyigit[4], and Mahmut Kus[5]

[1] *Vocational School of Technical Sciences, Department of Electricity and Energy, Konya Technical University, Konya, Turkey*
[2] *Department of Biotechnology, Faculty of Science, Selcuk University, Konya, Turkey*
[3] *Department of Chemistry, Faculty of Arts and Sciences, Yildiz Technical University, Istanbul, Turkey*
[4] *Department of Electronics and Automation, Vocational High School, Bilecik Seyh Edebali University, Bilecik, Turkey*
[5] *Department of Chemical Engineering, Konya Technical University, Konya, Turkey*

Received: 21 March 2023
Accepted: 10 July 2023
Published online: 29 July 2023

ABSTRACT

Efforts have been increased to create efficient photodiodes using a variety of interface layers such as organics, insulators, polymers, and metal oxides. Therefore, in this study, novel 4,5-diazafluorene ligands and their ruthenium (II) complexes were designed, synthesized, and elucidated by using ^{1}H NMR, FT-IR, UV-Vis, and mass spectroscopic (LC–MS) methods. The NMR, FT-IR, UV-Vis, and LCMS spectrometer results explained and confirmed the structure of the 4,5-diazafluorene ligands and their ruthenium (II) complexes. The obtained 4,5-diazafluorene ligands and their ruthenium (II) complexes were used as interfacial layer for Schottky type photodiode and characterized by $I-V$ measurements for various light power intensities. Various diode parameters such as rectification ratio, series resistance, and barrier height as well as ideality factor values were extracted and discussed in details. The results revealed that the fabricated Schottky type photodiodes with 4,5-diazafluorene ligands and their ruthenium (II) complex interlayers can be employed and improved for opto-electronic applications.

1 Introduction

The 4,5-diazafluorene (dafH) ligands were first reported in the late '70s by two-step modification from the 1, 10-phenanthroline molecule [1–4]. The dafH ligand can be considered as a 2, 2'-bipyridine (bpy) derivative containing a methylene bridge inserted between two pyridine rings (Fig. 1) [5]. The methylene group effectively binds the two pyridine rings, thus resulting in an extension between the N–N distance [5, 6]. This makes dafH and its derivatives

Address correspondence to E-mail: muratyildirim@selcuk.edu.tr; ibrahimerden@hotmail.com

https://doi.org/10.1007/s10854-023-10972-z

a weaker σ-binding ligand when compared to bpy. This increases or facilitates the dissociation of one of the donor N atoms. Thus, it provides a unique opportunity for the formation of unstable binuclear complexes that can be catalytically active [7]. Also, for many years, dafH ligands have been drawing attention by researchers in many fields such as cancer researches [8, 9], polymers [10, 11], organic electronics [12], sensors [13, 14], catalyst [15]. DafH derivatives are generally significantly lower than bpy in the spectrochemical series, which causes to occurring energetically lower state ligands.

Studies on effective and affordable optoelectronic devices that transform light into electrical energy are now crucial because of the world's rising energy needs. Metal-semiconductor contacts have attracted for optoelectronic applications such as photodiodes, photodetector, and phototransistors devices [16]. The most effective approach is to convert light intensity to an electrical signal with photodiodes. The characteristics of the photodiode affect how effectively the conversion process works. Due to the low mobility of the charge carriers in these materials, the active layer should be thin and typically less than 100 nm. Thinner layers provide more efficient charge transmission, but they reduce the amount of light absorbed [17]. To create a junction in photodiodes, metal-oxide semiconductors are typically placed on silicon (Si) substrates. In photodiode designs, a variety of oxide semiconductors have been employed [18]. Some of materials such as organic materials, polymers, metal oxides, or insulator layers can be inserted between the metal and semiconductor to improve performance of these devices [19–22]. According to literature, various material types have been used as interlayers to improve the durability, stability, and efficiency of heterojunctions [23, 24]. Thus, these devices can be more efficient and powerful for optoelectronic applications. Organic materials are appealing to a variety of fields and researchers because of their versatility, compatibility with the environment, and inexpensive and healthy behaviors [25]. Organic materials and polymers are emerging materials, which have gained vast attentions nowadays. Depending on the intended use, their optoelectronic properties can be easily modified by manipulating the molecule structure to enhance radiative recombination, charges transport, or photogeneration [26].

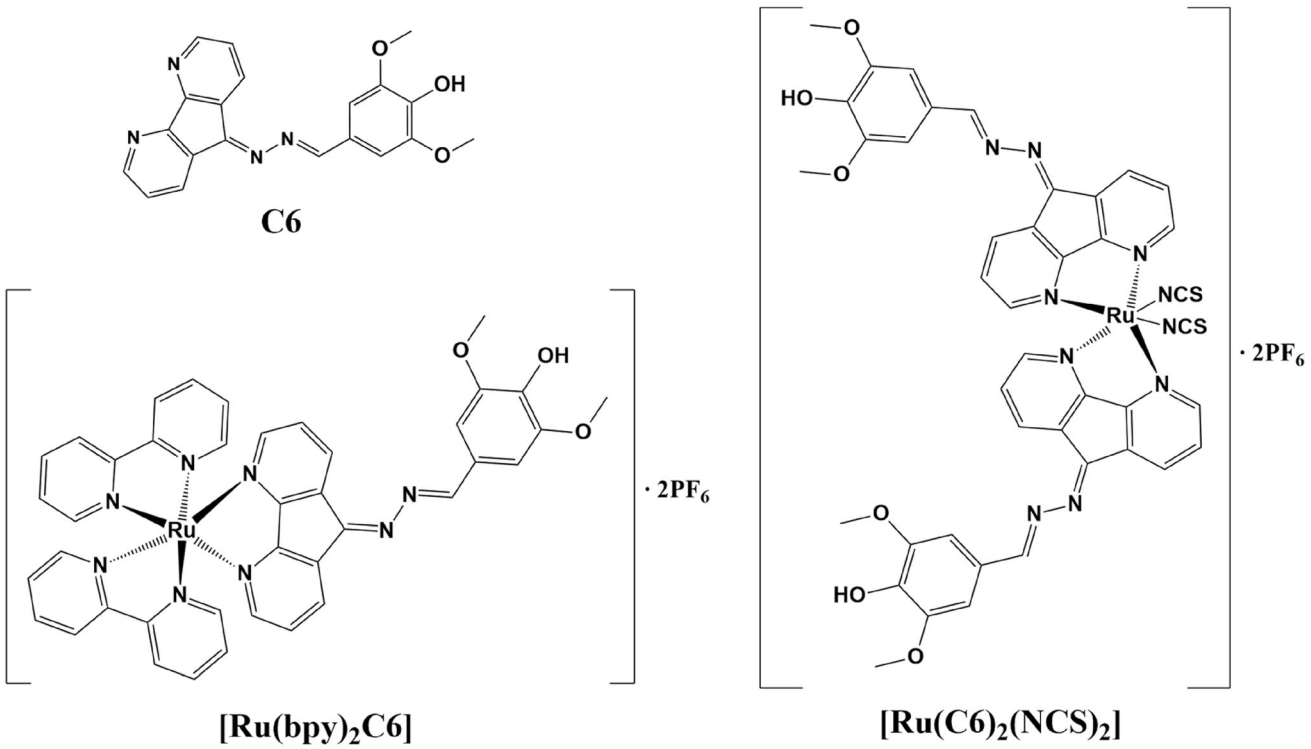

Fig. 1 Molecule structures of C6, $[Ru(bpy)_2C6]$ and $[Ru(C6)_2(NCS)_2]$

In this research, methoxy and hydroxyl functional groups containing aldehyde compound combined with hyrazone derivative of daf with two azomethine bonds. Both Ruthenium bipyridine and isothiocyanate complexes of novel ligand were prepared. Characterizations of compound were carried out by FT-IR, NMR, UV-vis, and LCMS methods. The synthesized methoxy and hydroxyl functional groups were used as interfacial layer between the Al and *p*-Si to investigate performance effect of the Schottky type photodiodes.

2 Experimental section

2.1 Chemicals

1, 10-phenanthroline monohydrate (Merck), syringaldehyde (Aldrich), hydrazine hydrate (Merck), all other chemicals were purchased from commercial sources and used as received without any further purification.

2.2 Synthesis

The precursors 4,5-diazafluorene-9-one (dafo), 4,5-diazafluorene-9-hydrazone (dafh), and cis-$(bpy)_2RuCl_2{\cdot}2H_2O$ were produced and purified in accordance with well-known literature [27, 28].

2.2.1 Synthesis of 4-(((5H-cyclopenta[1, 2-b:5,4-b′]dipyridin-5-ylidene)hydrazono)methyl)-2, 6-dimethoxyphenol (C6)

A 50 mL single-neck round-bottom flask was filled with the following ingredients: dafh (136.1 mg, 0.69 mmol), syringaldehyde (127.5 mg, 0.7 mmol), catalytic quantity of p-toluenesulfonic acid (PTSA), and 25 mL toluene. The mixture was then stirred at 105–115 °C under an argon atmosphere for 16 h. TLC kept track of how the reactions were progressing. After the solvent was reduced by half through rotary evaporation, the crude products were precipitated at room temperature, filtered through borosilicate glass D4 filters, purified twice with 10 mL of cold diethyl ether and 10 mL of cold water, and then dried in a vacuum for an entire night at 40 °C. 220 mg red solid product was obtained. Yield: % 91. FT-IR (ATR, cm^{-1}): 3400 − 2700 ν(broad, O–H), 1628 ν (9-position of dafH, C = N), 1601 and 1578 (C = N dafH), 1580 and 1499 ν(phenyl, C = C). ^1H NMR (500 MHz, DMSO) δ 8.86 (s, 1H), 8.74 (d, *J* = 25.4 Hz, 2H), 8.30 (s, 1H), 7.66–7.03 (m, 5H), 5.75 (s, 1H), 3.90 (s, 5H). LCMS-QTOF: m/z: 361.12 $[M + H]^+$.

2.2.2 Synthesis of [Ru(bpy)$_2$C6]

cis-$(bpy)_2RuCl_2$ (57.0 mg, 0.117 mmol), C6 (43.24 mg, 0.12 mmol), KPF_6 (44.17 mg, 0.24 mmol) and 15.0 mL methanol were added to 25.0 mL single-neck round-bottom flask and stirred at 60–65 °C under the argon atmosphere for 12 h. After the solvent was removed by rotary evaporation, the crude product was washed with 10.0 mL cold methanol twice times for removing excess of ligand and KPF_6; then product was dried in vacuum overnight at 40 °C. 60.0 mg red solid product was obtained. Yield: % 48 FT-IR (ATR, cm^{-1}): 3092 ν (Ph, C = H), 1738 ν (9-position of dafH, C = N), 1661. LCMS: m/z 919.0 $[M + H + PF_6]^+$, and [1064.1 $M + 2PF_6]^+$.

2.2.3 Synthesis of [Ru(C6)$_2$(NCS)$_2$]

$RuCl_3{\cdot}xH_2O$ (21.1 mg, 0.1018 mmol), C6 (73.36 mg, 0.203 mmol), a small amount of LiCl and 12 mL DMF were added to 25 mL single-neck round-bottom flask and stirred at 150–160 °C under the argon atmosphere for 8 h. After the color of the reaction mixture turned to violet, NH_4NCS (16 mg, 0.21 mmol), KPF_6 (38.6 mg, 0.21 mmol), 3 mL DMF were added to the flask and the reaction was continued for 12 h under the argon atmosphere at 150–160 °C. The solvent was removed by rotary evaporation, the crude product was washed with 10 mL cold methanol twice times for removing excess of ligand, NH_4NCS and KPF_6; then the product was dried in the vacuum overnight at 40 °C. 64.0 mg black solid product was obtained. Yield: % 51.0 FT-IR (ATR, cm^{-1}): 3500 − 2500 ν(broad, O–H), 3064 ν (Ph, C = H), 2101 and 1963 (-NCS), 1655 ν (9-position of Daf, C = N) and 1507. LC–MS: m/z 1084.1 $[M + 2H + PF_6]^+$, 1231.1 $[M + 4H + 2PF_6]^+$.

2.3 Fabrication of devices

Fabrication of the devices started with the slicing and cleaning of the *p*-type Si wafer. A one-side polished *p*-type Si wafer which had (100) crystalline orientation and 7.3×10^{15} cm^{-3} carrier concentrations was divided into 1×2 cm^2 pieces and then cleaned in

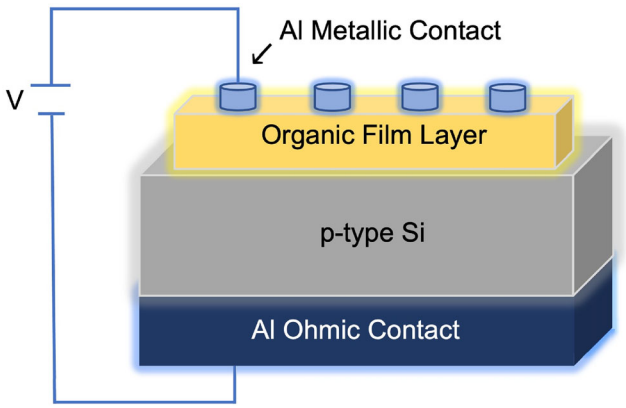

Fig. 2 Schematic illustration as well as measurement setup of the Al/[Ru(bpy)$_2$C6]/*p*-Si, Al/C6/*p*-Si and Al/[Ru(C6)$_2$(NCS)$_2$]/*p*-Si photodiodes

acetone, propanol, and distilled water by an ultrasonic cleaner for 30 min. Naturally composed SiO_2 layers were etched by using of the HF:H_2O (1:10) solution for 30 s. The pieces were immediately put inside a thermal evaporator arranged at 5×10^{-6} - Torr pressure to obtain back contact, and Al metal was evaporated as 150 nm thicknesses onto unpolished surfaces of the pieces. The prepared solutions of the C6, [Ru(bpy)$_2$C6] and [Ru(C6)$_2$(NCS)$_2$] in ethanol were coated on the wafer pieces by spin coating technique at 3000 rpm for 30 s. Organic film layers were coated again with 100 nm Al as patterned dots to obtain metallic contact by a hole array mask in thermal evaporator. Thus, Al/C6/*p*-Si, Al/[Ru(bpy)$_2$C6]/*p*-Si, and Al/[Ru(C6)$_2$(NCS)$_2$]/*p*-Si photodiodes were fabricated for the C6, [Ru(bpy)$_2$-C6], and [Ru(C6)$_2$(NCS)$_2$] inter layers. The schematic illustration as well as measurement system of the Al/C6/*p*-Si, Al/[Ru(bpy)$_2$C6]/*p*-Si and Al/[Ru(C6)$_2$(NCS)$_2$]/*p*-Si photodiodes have been shown in Fig. 2.

3 Results and discussion

3.1 Synthesis and characterization

FT-IR band changes in the functional groups of starting compounds and final products were used for monitoring of purities of compound and occurrence of reactions. The FT-IR spectrums of the phen, dafo, and dafh have been given in Fig. S1, S2, and S3, respectively. Firstly, dafo was obtained from phen by the reaction of potassium permanganate in basic aqueous media. As a result of reaction, oxidative ring contraction occurred, and we observed the carbonyl stretching band at 1715 cm^{-1}. In the next step, carbonyl functional group converted to hydrazone via the reaction of dafo with hydrazine hydrate in acidic medium. In the FT-IR spectrum, the disappearance of the peak of the carbonyl group at 1715 cm^{-1} in dafo and the peaks of the amine group between 3374 and 3305 cm^{-1} indicate that the dafh molecule was formed. In the ligand synthesis, condensation reaction of aldehyde unit of syringaldehyde with primary amine unit of dafh resulted Schiff base formation (Scheme 1). Toluene was used as a non-aqueous solvent with a high boiling point in order to obtain good yields in the Schiff base reaction. The disappearance of the amine group of Dafh at 3370, 3310 cm^{-1} and the carbonyl group of syringaldehyde at 1667 cm^{-1} as a result of the condensation reaction, and the formation of a band of weak azomethine stretching vibrations at 1628 cm^{-1} indicate the formation of the C6 compound (Fig. S5). The ^{1}H NMR spectrum of C6 is provided in Supplementary Information (Figures S6 and S7, respectively) and recorded in DMSO-d$_6$. The ^{13}C NMR spectrum of C6 was not recorded due to the poor solubility of the compounds in deuterated solvents. ^{1}H NMR of the C6 compound showed single peaks at 3.90 ppm of the − Me group and 5.75 ppm of the − OH group. In addition, multiplets seen between 8.83 and 6.97 ppm

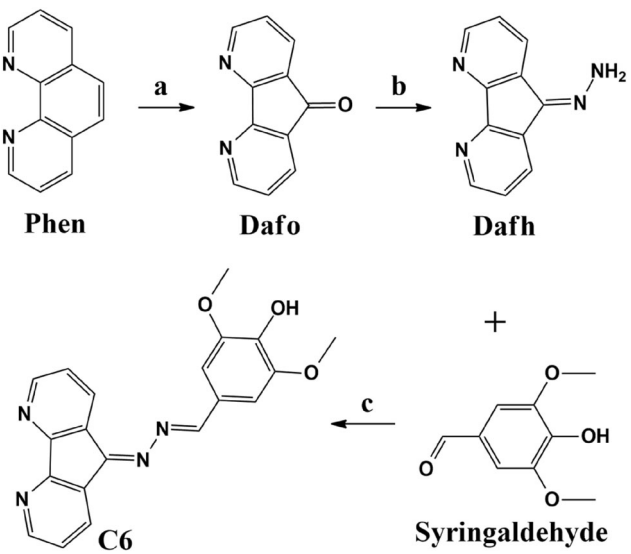

Scheme 1 The synthesis route of C6 ligand **a** $KMnO_4$, KOH, H_2O, Δ; **b** AcOH, NH_2NH_2, MeOH, 8 h; **c** Toluene, 16 h, PTSA, 105–115 °C

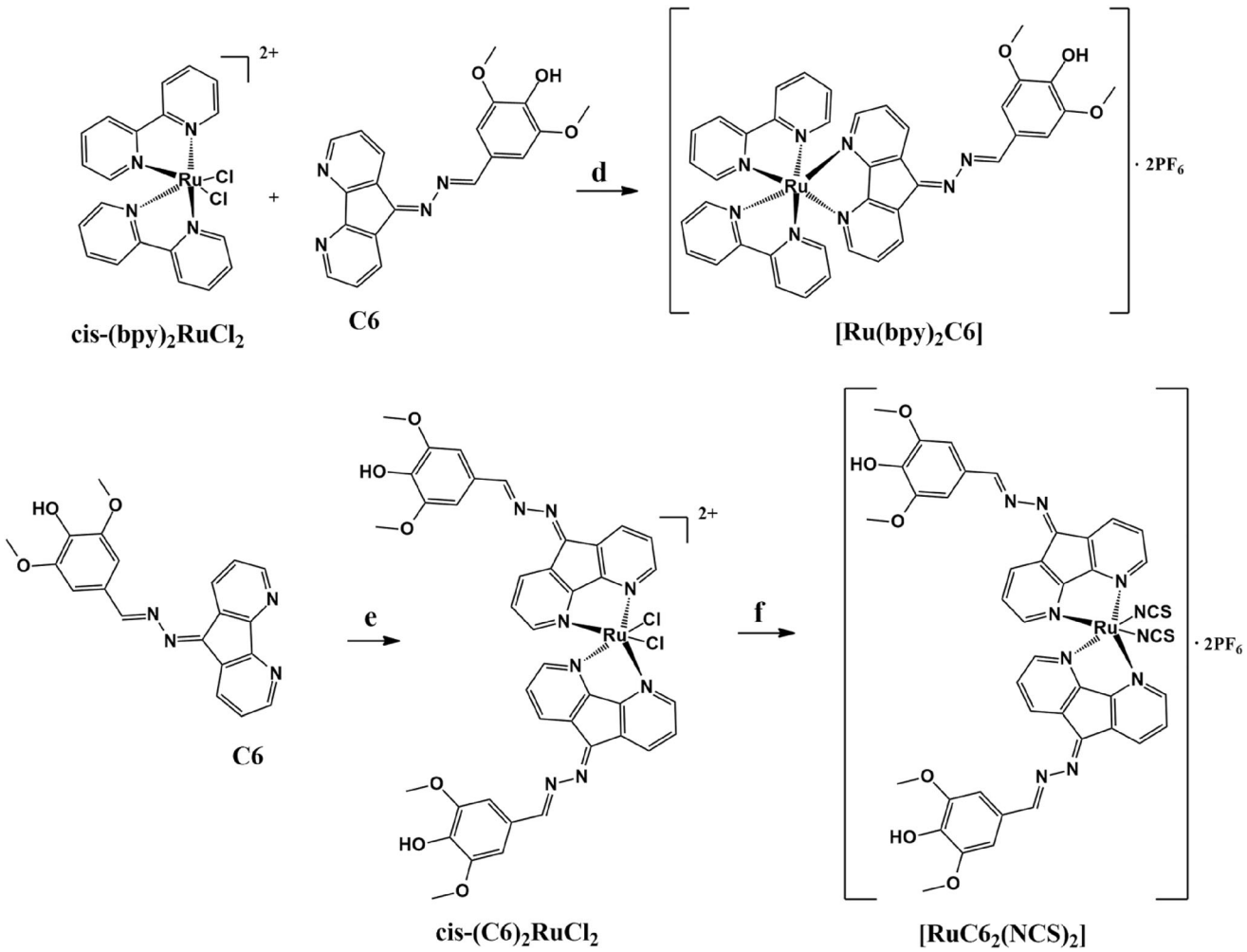

Scheme 2 The syntheses route of ruthenium bipyridine and isothiocyanate complexes **a** MeOH, 60–65 °C, 12 h **b** $RuCl_3 \cdot xH_2O$, LiCl, DMF, 150–160 °C, 8 h; **c** NH_4NCS, KFP_6, DMF, 150 °C, 12 h

the signals originated from the protons of the aromatic groups. The molecular ion peak of C6 was appeared at m/z: 362.12 $[M + H]^+$.

Ruthenium bipyridine complex was synthesized by reaction of C6 with *cis*-$(bpy)_2RuCl_2 \cdot 2H_2O$ 1:1 molar ratio in methanol. Ruthenium isothiocyanate complex of C6 was synthesized with two-step synthetic processes. Firstly, *cis*-$C6_2RuCl_2$ complex was synthesized by the reaction of $RuCl_3 \cdot xH_2O$ with C6 in 1:2 mol ratios. After the reaction mixture turned violet about at the end of 8 h, a little excess amount of NH_4NCS and KPF_6 from 1:2 mol ratio was added to the mixture. Then, the reaction was continued for 12 h until the color turned black and LiCl was used to prevent the dissociation of the Cl anion in the synthesis of the Cis-C62RuCl2 complex [21]. KPF6 was used as a complementary ion source in the precipitation of complex compounds (Scheme 2). The shifts in the FT-IR bands are important spectroscopic data for understanding metal-ligand coordination. In the characterization of the ruthenium bipyridine complex; While the stretch band belonging to the imine group was observed at 1628 cm^{-1} in compound C6, it shifted to 1738 cm^{-1} after the formation of Ru (II) complexes. In the characterization of Ruthenium isothiocyanate complex with FT-IR; The bands at 2101 and 1960 cm^{-1} belong to the -NCS group [29]. Mass analyzes are prominent for characterization of complexes, and LCMS was used for this purpose. A 3-min. direct infusion electrospray ionization mass spectrometry (DI-ESI-MS) method was applied in positive ion mode. Mass spectra were obtained by introducing samples to the MS in a mixture of 49.95% acetonitrile (HPLC grade), 49.95%

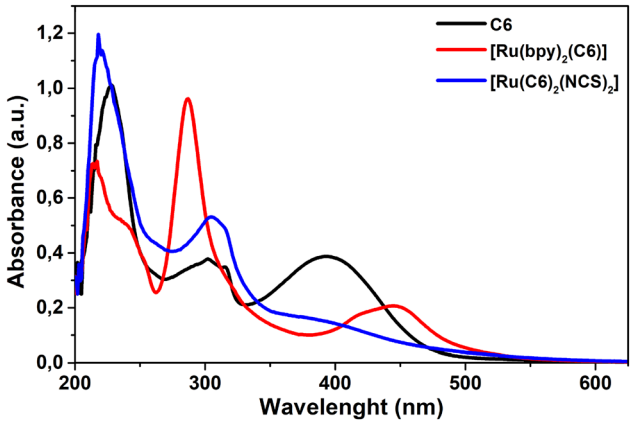

Fig. 3 UV-vis absorption spectra of the C6, $[Ru(bpy)_2C6]$ and $[Ru(C6)_2(NCS)_2]$

water (ultra-pure), and 0.1% formic acid (v/v) at a flow rate of 0.6 mL/min. Evidently; m/z 919.0 and 1064.1 are proved the formation of $[Ru(bpy)_2C6]$ complex. Clearly, m/z 1084.1 and 1231.1 are proved the formation of $[Ru(C6)_2(NCS)_2]$ complex. PF_6 anions were observed in mass spectra of each complex.

3.2 Optical properties

The electronic absorption spectra of C6 ligands and its Ru (II) complexes were measured in methanol (Fig. 3). Absorption peaks of C6 were observed at 228, 304, 394 nm associate with n-π*, n-σ* and π-π* transitions. Absorption peaks of Ru (II) bipyridine complex were observed at 216, 287, and 446 nm. Peak

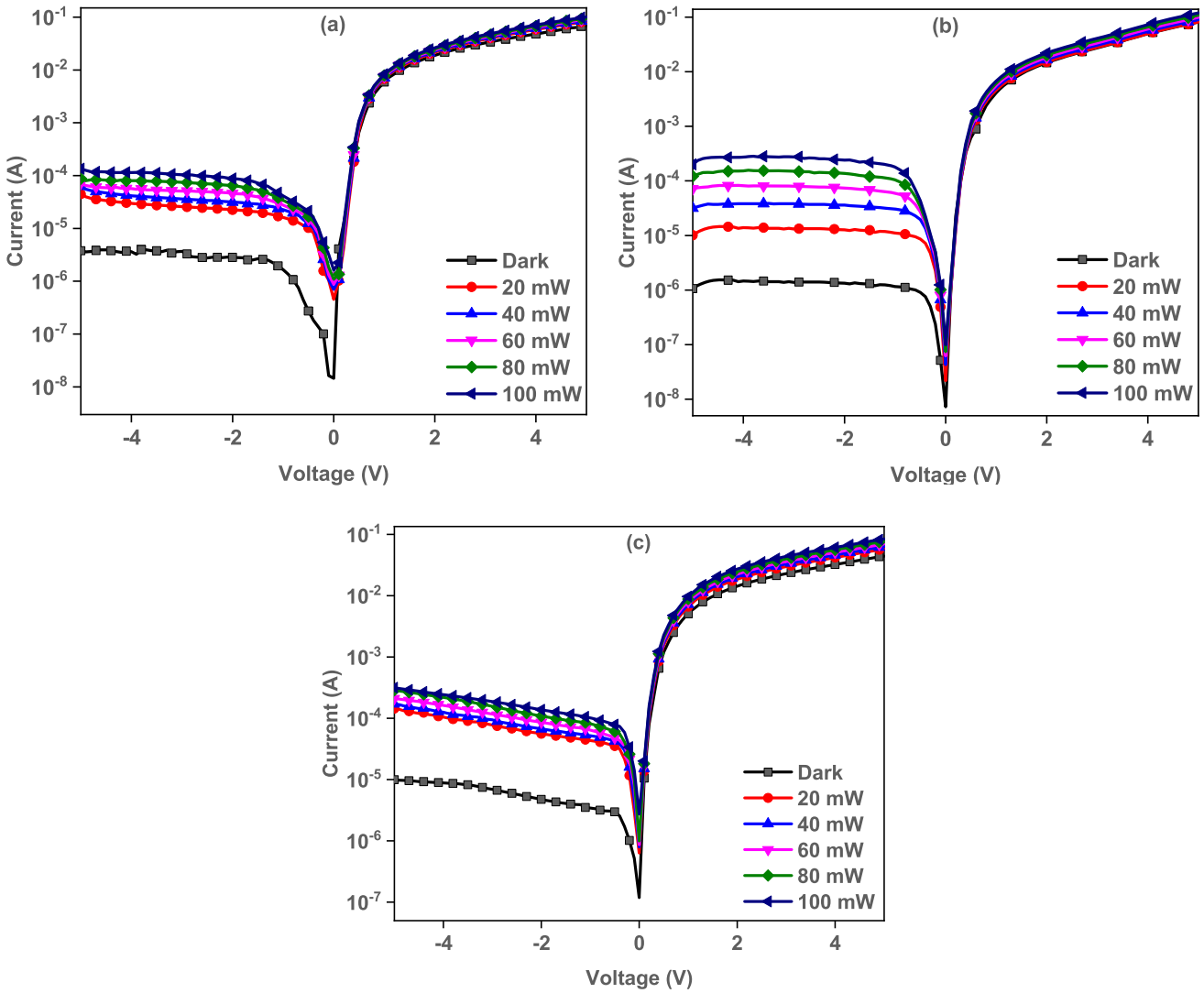

Fig. 4 The *I–V* characteristics of the **a** Al/C6/*p*-Si, **b** Al/$[Ru(bpy)_2C6]$/*p*-Si, and Al/$[Ru(C6)_2(NCS)_2]$/*p*-Si photodiodes for various light power illumination intensities at per cm^2

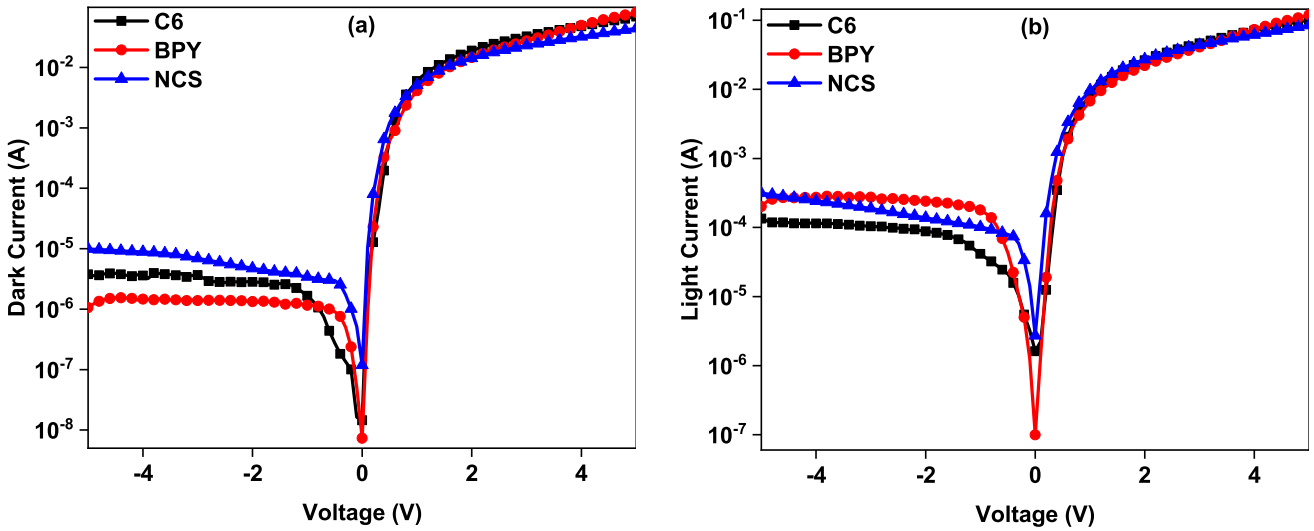

Fig. 5 Comparison the *I–V* characteristics of the Al/C6/*p*-Si, Al/[Ru(bpy)$_2$C6]/*p*-Si, and Al/[Ru(C6)$_2$(NCS)$_2$]/*p*-Si photodiodes **a** dark and **b** 100 mW/cm^2 light power illumination intensity

at 446 nm is associate with metal-to-ligand charge-transfer (MLCT) transitions in Ru (II) bipyridine complexes. Absorption peaks of Ru (II) isothiocyanate complex were observed at 218, 305, 373 nm. Peak at 373 is associate with metal-to-ligand charge-transfer (MLCT) transitions and this transition band extends to 573 nm.

3.3 Electrical properties

The fabricated Al/C6/*p*-Si, Al/[Ru(bpy)$_2$C6]/*p*-Si and Al/[Ru(C6)$_2$(NCS)$_2$]/*p*-Si devices were characterized by *I–V* measurements at different light power illumination levels. The light power illumination dependent *I–V* characteristics of the Al/C6/*p*-Si, Al/[Ru(bpy)$_2$C6]/*p*-Si, and Al/[Ru(C6)$_2$(NCS)$_2$]/*p*-Si photodiodes have been displayed in Fig. 4a, b, and c, respectively. The photodiodes exhibited good photodiode behavior at reverse biases because the current clearly increased with increasing light power intensity. The reverse current increased 10 times with 20 mW/cm^2 for all devices, and then they exhibited slowly increment for other light power intensities. The Al/[Ru(bpy)$_2$C6]/*p*-Si photodiode is the best photoconductive behavior among the other obtained devices. In the case of forward biases, generally current increased slightly with increasing light power intensity. Having different current profiles for various interlayered devices can be attributed to effect of the type or formation of the interfacial layer material between the metal and semiconductor [20, 30].

The obtained devices can be clearly used for photodetector applications due to increasing current at reverse biases with increasing light power intensity according to dark condition [31]. However, Al/[Ru(bpy)$_2$C6]/*p*-Si device exhibited good performance for increasing light power. The other devices clearly did not show high level increase for increasing light power intensity. These results can be attributed to chemical structure of the interfacial layer as well as current saturation level.

The various organic interlayered photodiodes were compared for the performance under dark and 100 mW/cm^2 light power intensity. Figure 5a and b show the comparison of the Al/C6/*p*-Si, Al/[Ru(bpy)$_2$C6]/*p*-Si, and Al/[Ru(C6)$_2$(NCS)$_2$]/*p*-Si photodiodes in the case of dark and 100 mW/cm^2 light power intensity. According to Fig. 5, the Al/[Ru(bpy)$_2$C6]/*p*-Si photodiode exhibited least current under dark and highest current under 100 mW/cm^2 light power intensity.

The rectifying ratio (*RR*) is important for diodes to show their ability against to flowing current, and it is calculated by the ratio of the forward current to reverse current ($RR = I_{forward}/I_{reverse}$) at same voltage value [32]. Figure 6 exhibits light power intensity dependent *RR* values (at 3 V) for the Al/C6/*p*-Si, Al/[Ru(bpy)$_2$C6]/*p*-Si, and Al/[Ru(C6)$_2$(NCS)$_2$]/*p*-Si photodiodes. The *RR* values were calculated as 8.90×10^3, 1.98×10^4, and 3.33×10^3 for the Al/C6/

p-Si, Al/[Ru(bpy)$_2$C6]/*p*-Si, and Al/[Ru(C6)$_2$(-NCS)$_2$]/*p*-Si photodiodes, respectively. However, the *RR* values decreased and then stayed almost constant with increasing light power intensity due to increasing reverse bias currents.

In a study by Yuan, a high rectification ratio of 607 at ± 1.65 V and a low turn-on voltage of 0.9 V were achieved for the device in dark, such high RR was ascribed to high electron mobility of ZnO NPs and large ZnO NPs/SubPc interface in the device [33]. In another study by Yuan, rectification ratio of 3211 at 2 V and a low turn-on voltage of 0.5 V in the dark were achieved [34]. Gencer Imer et al. received good rectification ratio of 2.4×10^4 at ± 7 V using Al/Ru(II) complex/p-Si photodiode [35]. In a study by Hussaini et al., RR of 36,800 were achieved using $LiCoO_2$ interlayer in Schottky photodiode structure [36]. In another study by Kocyigit et al., rectification ratios were achieved between 42 and 45 for Al/Cd-complex/p-Si and Al/Co-complex/p-Si photodiode devices [37]. Herein, the obtained results in this study could hold an extremely good record compared to literatures.

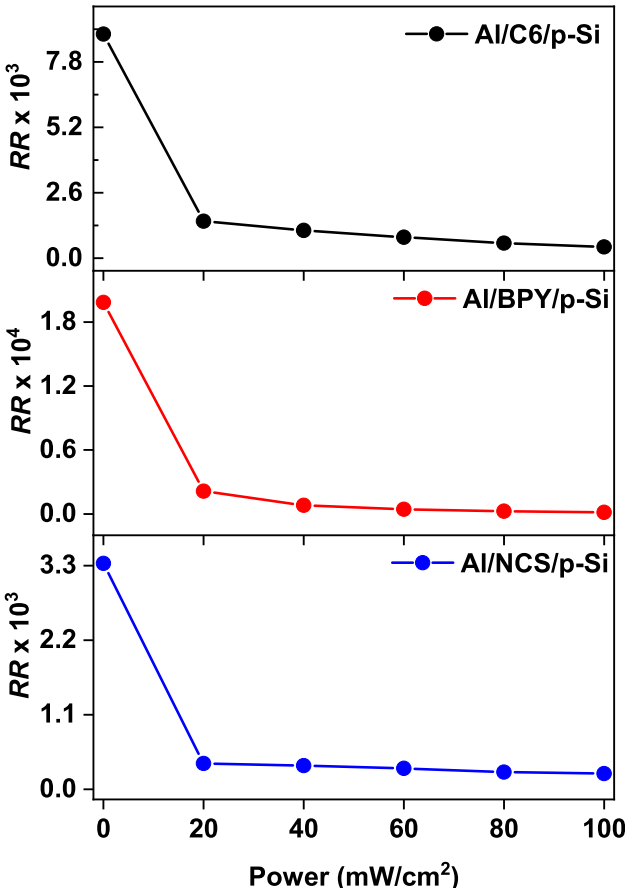

Fig. 6 The *RR* values versus light power intensity of the Al/C6/*p*-Si, Al/[Ru(bpy)$_2$C6]/*p*-Si, and Al/[Ru(C6)$_2$(NCS)$_2$]/*p*-Si photodiodes

To better understanding of device characteristics, the diode parameters such as ideality factor (n), barrier height (φ_b), and series resistance (R_s) can be extracted from the *I–V* characteristics. There are three general methods to determine these parameters: thermionic emission, Cheung, and Norde methods. The current (I) is given by next equation according to thermionic emission theory:

$$I = I_0 \exp\left(\frac{qV}{nkT}\right)\left[1 - \exp\left(-\frac{qV}{nkT}\right)\right], \quad (1)$$

where I_0 exhibits saturation current and addressed by next equation:

$$I_0 = AA^*T^2\exp\left(-\frac{q\varphi_b}{kT}\right), \quad (2)$$

where k and q show Boltzmann's constant and charge of the electron. While the A displays the diode area, T and A^* represent the measurement temperature and Richardson constant (32 A/cm^{2}K^2 for *p*-type Si), respectively. The n and φ_b are accounted by following formulas from the slope of the second linear region and the saturation current at the *I–V* curve:

Table 1 Various diode parameters of the Al/C6/*p*-Si, Al/BPY/*p*-Si, and Al/NCS/*p*-Si photodiodes

Interface type	Saturation current (I_0)	n (*I–V*) –	n Cheung –	Φ_b (*I–V*) (eV)	Φ_b Cheung (eV)	Φ_bNorde (eV)	R_s Cheung (Ω ($H(I)$))	Cheung (Ω ($d\ln(I)$))	R_sNorde (Ω)
C6	2.92×10^{-7}	3.00	3.06	0.65	0.64	0.71	67.59	74.46	58.26
[Ru(bpy)$_2$C6]	3.00×10^{-6}	3.51	3.52	0.62	0.63	0.64	74.32	95.22	38.69
[Ru(C6)$_2$(NCS)$_2$]	6.75×10^{-6}	3.69	3.77	0.57	0.58	0.61	96.33	102.09	30.18

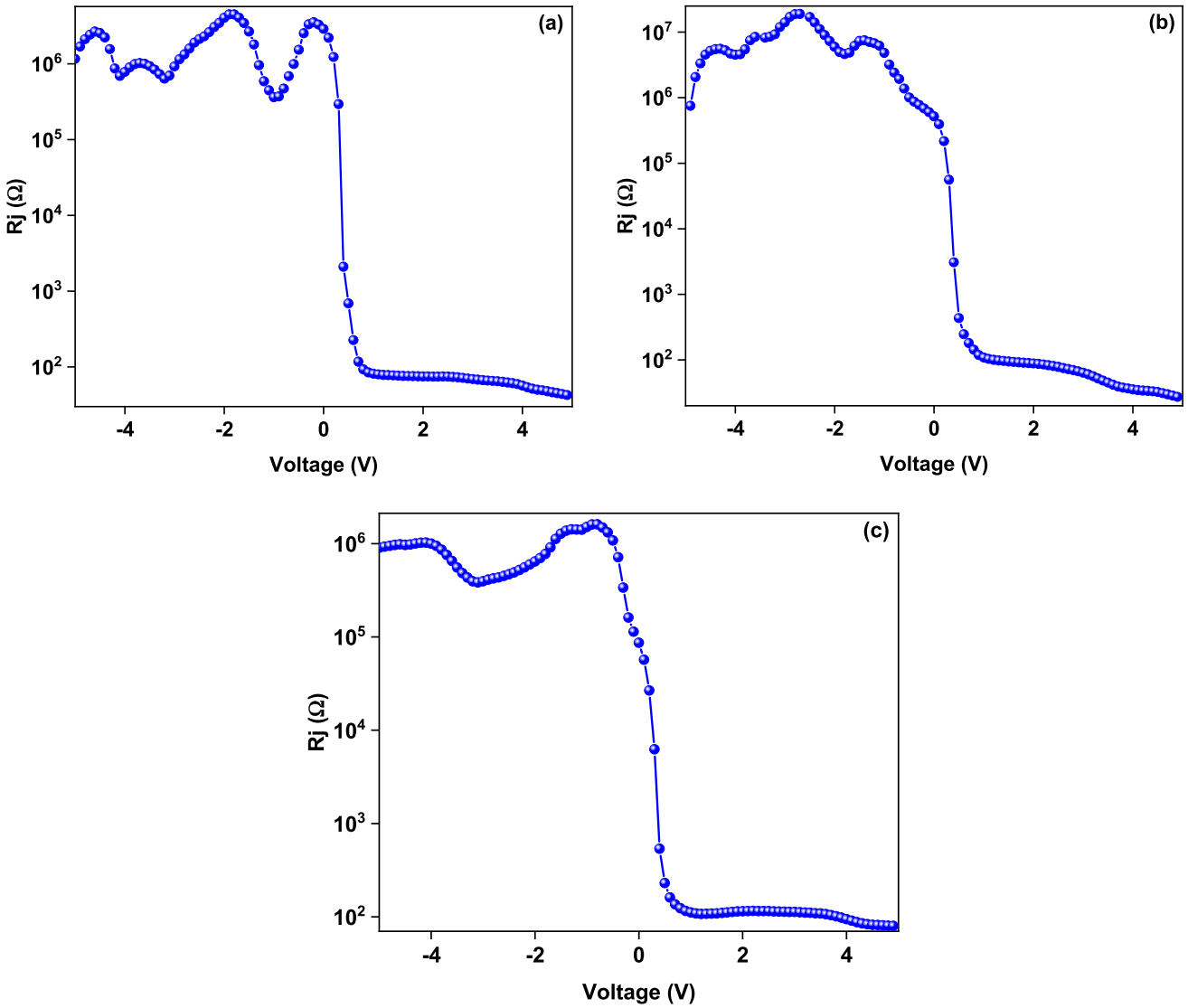

Fig. 7 The R_j changes of the **a** Al/C6/*p*-Si, **b** Al/[Ru(bpy)$_2$C6]/*p*-Si, and Al/[Ru(C6)$_2$(NCS)$_2$]/*p*-Si photodiodes depending on the applied voltage

$$n = \frac{q}{kT}\left(\frac{dV}{d\ln I}\right) \tag{3}$$

$$\phi_b = \frac{kT}{q}\ln\left(\frac{A^*AT^2}{I_0}\right) \tag{4}$$

The n and φ_b values calculated from the thermionic emission theory were tabulated in Table 1 for the Al/C6/*p*-Si, Al/[Ru(bpy)$_2$C6]/*p*-Si, and Al/[Ru(C6)$_2$(NCS)$_2$]/*p*-Si photodiodes. All the devices has higher ideality factor values than unity due to interface states, barrier inhomogeneity, non-uniform interlayer [38, 39]. The Al/C6/*p*-Si photodiode has highest barrier height and lowest ideality factor value. The ideality factor and barrier height values changed depending on the organic complex of [Ru(bpy)$_2$C6] and [Ru(C6)$_2$(NCS)$_2$] due to changing charge carriers and interface states [40].

The junction resistance (R_j) is important parameter to better understanding of the diode characteristics and obtained from *I*–*V* characteristics [41]. The R_j has series resistance (R_s) and shunt resistance (R_{sh}) components at forward and reverse biases, respectively [16]. The R_j is given by next equation from the *I*–*V* measurements:

$$R_j = \frac{\partial V}{\partial I} \tag{5}$$

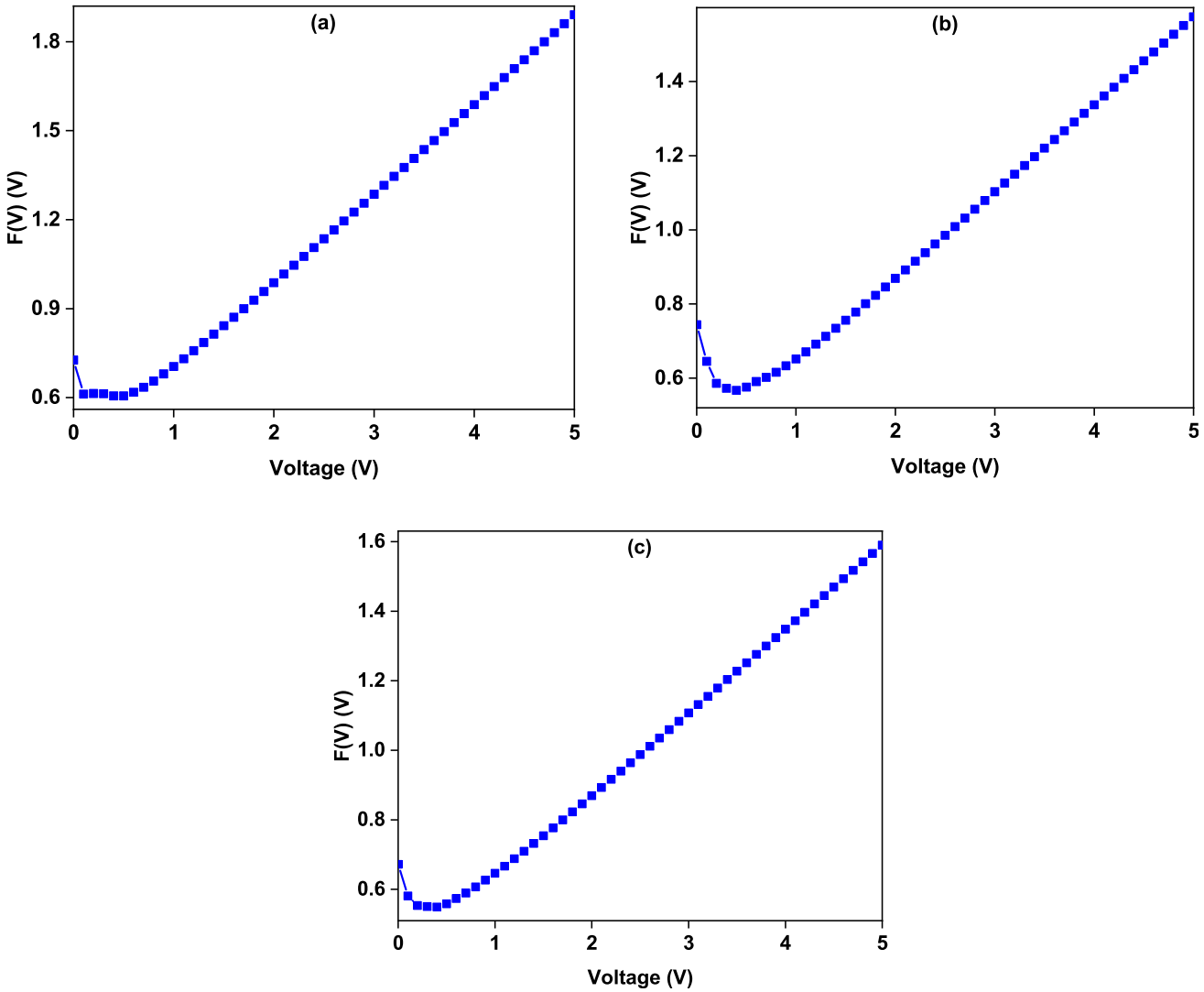

Fig. 8 The Cheung plots of the **a** Al/C6/*p*-Si, **b** Al/[Ru(bpy)$_2$C6]/*p*-Si, and Al/[Ru(C6)$_2$(NCS)$_2$]/*p*-Si photodiodes

R_j–V plots of the Al/C6/*p*-Si, Al/[Ru(bpy)$_2$C6]/*p*-Si, and Al/[Ru(C6)$_2$(NCS)$_2$]/*p*-Si photodiodes have been shown in Fig. 7a, b, and c, respectively. The photodiodes clearly have R_{sh} and R_s regions at reverse and forward biases, respectively. While the forward bias regions reveal that all devices have low series resistance than 100 Ω, reverse bias region display that, all photodiodes have 10^6 Ω levels shunt resistance. These values are good agreement with the proper optoelectronic devices [42]. The Al/[Ru(bpy)$_2$C6]/*p*-Si photodiode has highest shunt resistance and lowest series resistance according to R_j–V plots.

The barrier height and series resistance values can be calculated by Norde technique. The Norde technique is used Norde Function to obtain device parameters, and it is given by following equation [43]:

$$F(V) = \frac{V}{\gamma} - \frac{kT}{q} ln\left(\frac{I(V)}{AA^*T^2}\right), \tag{6}$$

where $I(V)$ exhibits current of related voltage. γ shows closest integer higher than n. Norde function is reorganized to calculate the φ_b and R_s values, and they are given by next equations:

$$\varphi_b = F(V_0) + \left[\frac{V_0}{\gamma} - \frac{kT}{q}\right] \tag{7}$$

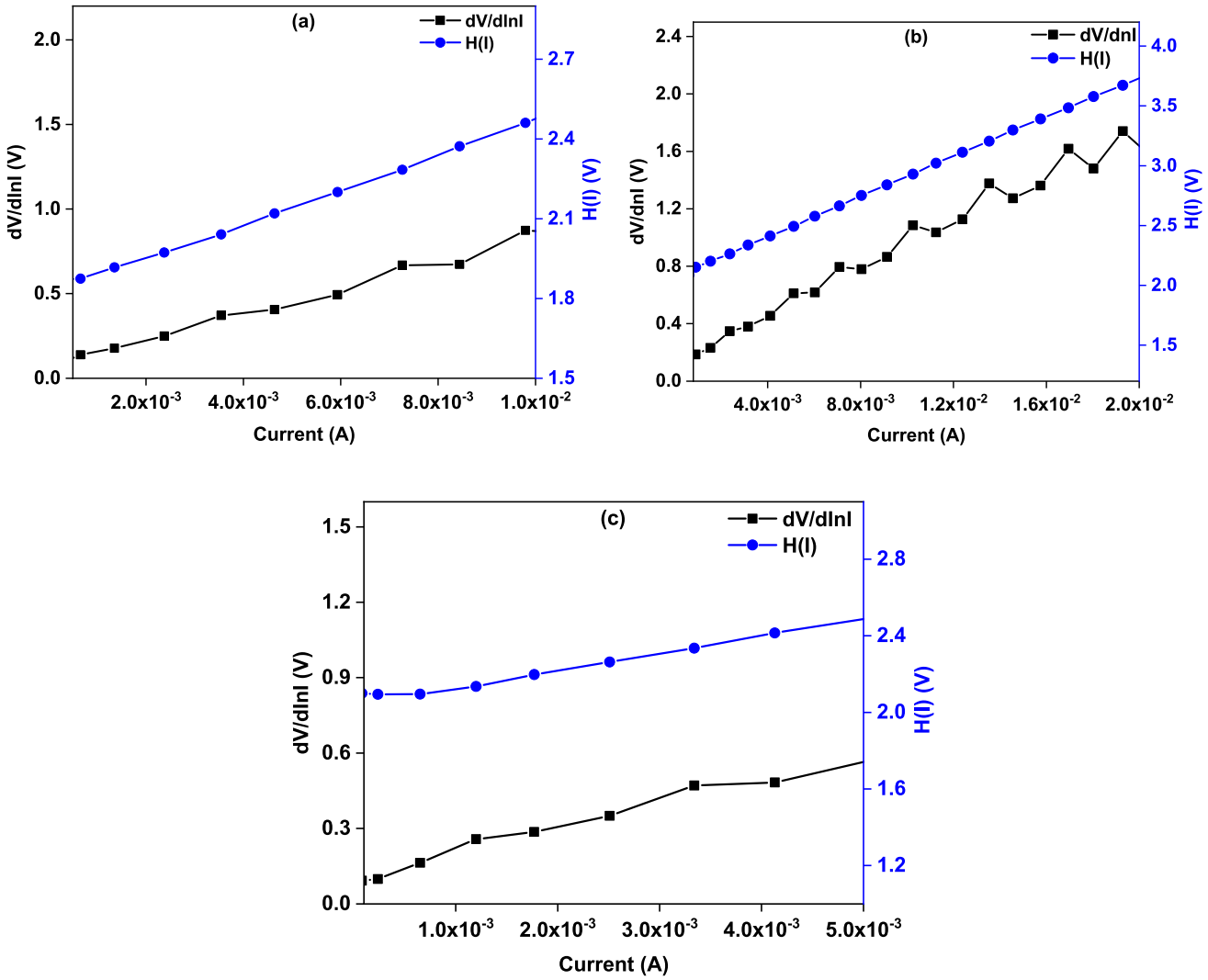

Fig. 9 The Cheung plots of the **a** Al/C6/*p*-Si, **b** Al/[Ru(bpy)$_2$C6]/*p*-Si, and Al/[Ru(C6)$_2$(NCS)$_2$]/*p*-Si photodiodes

$$R_s = \frac{\gamma - n\mathrm{kT}}{I}\frac{}{\mathrm{q}}, \tag{8}$$

where V_0 represents the minimum voltage value related minimum *F(V)*. *F(V)* versus *V* plots of the Al/C6/*p*-Si, Al/[Ru(bpy)$_2$C6]/*p*-Si, and Al/[Ru(C6)$_2$(NCS)$_2$]/*p*-Si photodiodes have been displayed in Fig. 8a, b, and c, respectively. The photodiodes have exhibited normal Norde plots, and thus, the φ_b and R_s values can be calculated by using Norde plot [44]. The φ_b and R_s values have been listed in Table 1 for each photodiode. The calculated R_s values highlight that all photodiodes have low series resistance. The φ_b values obtained from Norde technique are in well harmony with the thermionic emission φ_b values. Small differences can be dependent to approximation differences between techniques [45]. Cheung technique are also used nonlinear region of forward bias *I–V* curve to calculate ideality factor, series resistance as well as barrier height of the diodes [46]. There are two Cheung functions, and they are expressed by next equations:

$$\frac{dV}{d(lnI)} = IR_s + n\frac{\mathrm{kT}}{\mathrm{q}} \tag{9}$$

$$H(I) = V - n\left(\frac{\mathrm{kT}}{\mathrm{q}}\right)ln\left(\frac{I}{AA^*T^2}\right), \tag{10}$$

where *H(I)* can be reorganized to following equation:

$$H(I) = IR_s + n\varphi_b \tag{11}$$

Equations 9 and 11 clearly show the linear equation for the *dV/d*(ln*I*) and *H(I)* functions for the current variable. While the intercepts reveals the *n* from

$dV/d(\ln I)$ and φ_b from $H(I)$ functions, the slops of the these plots give the R_s values for two functions [47, 48]. Figure 9a, b and c exhibit the Chung plots of the Al/C6/*p*-Si, Al/[Ru(bpy)$_2$C6]/*p*-Si, and Al/[Ru(C6)$_2$(NCS)$_2$]/*p*-Si photodiodes, respectively. Some deviations from linearity for Cheung plots can be seen owing to the interfacial layer effect. The n, φ_b and R_s values have been given in Table 1 for the Al/C6/*p*-Si, Al/[Ru(bpy)$_2$C6]/*p*-Si, and Al/[Ru(C6)$_2$(NCS)$_2$]/*p*-Si photodiodes.

The series resistance values of each photodiode obtained by two Cehung functions are in good agreement with each other, and this result confirms the consistency of the Cheung method. The comparison of the diode parameters with the other techniques reveals that the obtained diode parameters are close each other and can be accepted for comparison. The small differences can be dependent upon the approximation type as well as non-ideal diode structure or interfacial organic layers [49].

4 Conclusion

In this study, a novel 4,5-diazafluorene ligands and their ruthenium (II) complexes were successfully synthesized and characterized by using ^{1}H NMR, FT-IR, UV-Vis and mass spectroscopic (LC–MS) methods. The FT-IR, NMR, UV-Vis, and LCMS spectrometer results explained and confirmed the structure of the 4,5-diazafluorene ligands and their ruthenium (II) complexes.

The FT-IR and NMR results confirmed step by step synthetization of 4,5-diazafluorene ligands and their ruthenium (II) complexes. The UV-Vis spectrometer revealed absorption peaks of C6 ligands and Ru (II) complexes for various peak region and transitions. The LC–MS results showed formation of Ru (II) complexes as well as PF_6 anions. The effects of the C6 ligands and Ru (II) complexes between the Al and *p*-Si on Schottky type photodiode behaviors were characterized by *I–V* measurements for various light power intensities. While the ideality factor values of the Al/C6/*p*-Si, Al/[Ru(bpy)$_2$C6]/*p*-Si, and Al/[Ru(C6)$_2$(NCS)$_2$]/*p*-Si photodiodes were obtained as 3.00, 3.51, and 3.69, barrier height values were calculated as 0.65, 0.62, and 0.57 eV, respectively. The *RR* values were obtained as around 10^3–10^4 levels. The junction resistance plots revealed that the devices had low series resistance and high shunt resistance values. The C6 ligands and Ru (II) complexes can be found applications in Schottky type photodiodes.

Acknowledgements

We would like to state that the data used in this article are derived from Esma Yenel's and Caner Cebeci's PhD theses at Yıldız Technical University. We also would like to thank Ph.D. Tayfun Acar for his support in the mass analyzes of Ruthenium complexes.

Author contributions

EY was involved in conceptualization, investigation, experiments, methodology, writing the original draft, and corrections. MY was involved in characterization, and reviewing. CC contributed to writing, and editing. IE was involved in reviewing, and editing. AK contributed to experiments, characterization, writing the original draft, and corrections. MK contributed to reagents/materials/analysis tools, and reviewing.

Funding

This work was supported by The Scientific and Technological Research Council of Turkey (TUBITAK) Ph.D. Scholarship Program in Priority Areas (2211/C) and Council of Higher Education (YOK) Ph.D. Scholarship Program (100/2000) and partially supported by Selçuk University BAP office with 21401060 Project Number.

Data availability

The data that support the findings of this study are available from the corresponding author upon reasonable request.

Declarations

Conflict of interest The authors declare no conflict of interest.

Supplementary Information: The online version contains supplementary material available at https://doi.org/10.1007/s10854-023-10972-z.

References

1. K. Kloc, J. Mlochowski, Z. Szulc, J. Für. Prakt. Chem. **319**, 959 (1977)
2. J. Mlochowski, K. Kloc, Z. Szulc, Heterocycles. **9**, 849 (1978)
3. J. Druey, P. Schmidt, Helv. Chim. Acta. **33**, 1080 (1950)
4. G.E. Inglett, G. Frederick Smith, J. Am. Chem. Soc. **72**, 842 (1950)
5. V.T. Annibale, D. Song, Dalt. Trans. **45**, 32 (2016)
6. G.L. Lu, C.L. Ho, Q. Wang, W.Y. Wong, C.H. Chui, R.S.M. Wong, R. Gambari, F.Y. Lau, M.C.W. Yuen, C.S.W. Tong, A.K.W. Chan, J.C.O. Tang, K.P. Ho, G.Y.M. Cheng, Aust. J. Chem. **61**, 975 (2008)
7. R.A. Klein, P. Witte, R. van Belzen, J. Fraanje, K. Goubitz, M. Numan, H. Schenk, J.M. Ernsting, C.J. Elsevier, Eur. J. Inorg. Chem. **1998**, 319 (1998)
8. X. Wen, Y. Wu, Y. Tanaka, A. Awadasseid, H. Tao, W. Zhang, Life Sci. **269**, 119066 (2021)
9. K. Zhou, J. Liu, X. Xiong, M. Cheng, X. Hu, S. Narva, X. Zhao, Y. Wu, W. Zhang, Eur. J. Med. Chem. **178**, 484 (2019)
10. B. Deng, S. Zhang, C. Liu, W. Li, X. Zhang, H. Wei, C. Gong, RSC Adv. **8**, 194 (2018)
11. H. Li, B. Fan, D. Sun, J. Macromol. Sci. Part. A Pure Appl. Chem. **58**, 811 (2021)
12. Y. Yu, L.-Y. Bian, J.-G. Chen, Q.-H. Ma, Y.-X. Li, H.-F. Ling, Q.-Y. Feng, L.-H. Xie, M.-D. Yi, W. Huang, Y. Yu, L. Bian, J. Chen, Q. Ma, Y. Li, H. Ling, Q. Feng, L. Xie, M. Yi, W. Huang, Adv. Sci. **5**, 1800747 (2018)
13. H. Li, J. Wang, S. Zhang, C. Gong, F. Wang, RSC Adv. **8**, 31889 (2018)
14. S. Ghosh, A.S. Alghunaim, M.H. Al-Mashhadani, M.P. Krompiec, M. Hallett, I.F. Perepichka, J. Mater. Chem. C **6**, 3762 (2018)
15. J.N. Jaworski, C.V. Kozack, S.J. Tereniak, S.M.M. Knapp, C.R. Landis, J.T. Miller, S.S. Stahl, J. Am. Chem. Soc. **141**, 10462 (2019)
16. A. Kocyigit, M. Yilmaz, S. Aydogan, Ã. İncekara, H. Kacus, Mater. Sci. Semicond. Proc. **135**, 106045 (2021)
17. T. Nyberg, Synth. Met. **140**, 281 (2004)
18. M. Yıldırım, A. Kocyigit, Appl. Phys. A **128**, 700 (2022)
19. Z. Orhan, M. Yilmaz, S. Aydogan, M. Taskin, U. Incekara, Optik (Stuttg). **241**, 167069 (2021)
20. Y.J. Choi, H.J. Woo, S. Kim, J. Sun, M.S. Kang, Y.J. Song, J.H. Cho, J. Ind. Eng. Chem. **89**, 233 (2020)
21. X. Zou, Y. Li, G. Tang, P. You, F. Yan, Small. **15**, 1901004 (2019)
22. N.A. Al-Ahmadi, Mater. Res. Expr. **7**, 032001 (2020)
23. D.E. Yıldız, J. Mater. Sci. Mater. Electron. **29**, 17802 (2018)
24. D.E. Yildiz, H.H. Gullu, A. Sarilmaz, F. Ozel, A. Kocyigit, M. Yildirim, J. Mater. Sci. Mater. Electron. **31**, 935 (2020)
25. J.S. Chang, A.F. Facchetti, R. Reuss, IEEE J. Emerg. Sel. Top. Circ. Syst. **7**, 7 (2017)
26. K.-J. Baeg, M. Binda, D. Natali, M. Caironi, Y.-Y. Noh, Adv. Mater. **25**, 4267 (2013)
27. B.P. Sullivan, D.J. Salmon, T.J. Meyer, Inorg. Chem. **17**, 3334 (2002)
28. M.S. Deshpande, A.S. Kumbhar, J. Chem. Sci. **117**, 153 (2016)
29. M.K. Nazeeruddin, A. Kay, I. Rodicio, R. Humphry-Baker, E. Müller, P. Liska, N. Vlachopoulos, M. Grätzel, J. Am. Chem. Soc. **115**, 6382 (1993)
30. J. Pan, W. Deng, X. Xu, T. Jiang, X. Zhang, J. Jie, Chin. Phys B **28**, 038102 (2019)
31. M. İlhan, M.M. Koç, B. Coşkun, M. Erkovan, F. Yakuphanoğlu, J. Mater. Sci. Mater. Electron. **32**, 2346 (2021)
32. A. Barkhordari, S. Ozcelik, Å. Altindal, G. Pirgholi-Givi, H. Mashayekhi, Y. Azizian-Kalandaragh, Phys. Scr. **96**, 085805 (2021)
33. Z. Yuan, P.E. Low-Dimensional, Syst. Nanostruct. **56**, 160 (2014)
34. Z. Yuan, J. Yu, W. Ma, Y. Jiang, Appl. Phys. A **106**, 511 (2012)
35. A. Gencer Imer, A. Dere, A.G. Al-Sehemi, O. Dayan, Z. Serbetci, A.A. Al-Ghamdi, F. Yakuphanoglu, Appl. Phys. A **125**, 204 (2019)
36. A.A. Hussaini, M.O. Erdal, K. Doğan, M. Koyuncu, M. Yildirim, Appl. Phys. A **129**, 100 (2023)
37. A. Kocyigit, A.A. Hussaini, M. Yıldırım, D.A. Kose, D.E. Yıldız, Appl. Organomet. Chem. **36**, 6879 (2022)
38. Ã. Güllü, S. Asubay, Å. Aydoğan, A. Türüt, Phys. E Low-Dimens. Syst. Nanostruct. **42**, 1411 (2010)
39. I. Orak, A. Kocyigit, A. Turut, J. Alloys Compd. **691**, 873 (2017)
40. A. Kocyigit, Ä. Karteri, I. Orak, S. Uruş, M. Çaylar, Phys. E Low-Dimens. Syst. Nanostruct. **103**, 452 (2018)
41. L.D. Rao, V.R. Reddy, in *AIP Conf. Proc* (AIP Publishing LLC, 2016), p. 120020
42. Ä. Taşçıoğlu, W.A. Farooq, R. Turan, Å. Altındal, F. Yakuphanoglu, J. Alloys Compd. **590**, 157 (2014)
43. H. Norde, J. Appl. Phys. **50**, 5052 (1979)
44. S. Sen, N.B. Manik, J. Phys. Commun. **5**, 095010 (2021)
45. M. Yilmaz, A. Kocyigit, B.B. Cirak, H. Kacus, U. Incekara, S. Aydogan, Mater. Sci. Semicond. Process. **113**, 105039 (2020)

46. S.K. Cheung, N.W. Cheung, Appl. Phys. Lett. **49**, 85 (1986)
47. A. Kaymaz, E.E. Baydilli, H.U. Tecimer, A. Altındal, Y. Azizian-Kalandaragh, Radiat. Phys. Chem. **183**, 109 (2021)
48. A. Kocyigit, Ä. Orak, J. Inst. Sci. Technol. **6**, 57 (2016)
49. A. Tataroğlu, Å. Altındal, Y. Azizian-Kalandaragh, Phys. B Condens. Matter. **576**, 411733 (2020)